Geophys. J. Int. (2009) **177,** 145–160 doi: 10.1111/j.1365-246X.2009.04042.x

Seismic structure in and around the source area of the 2004 mid-Niigata, Japan, earthquake: 3-D waveform modelling based on local tomography images

Reiko Tajima,[1] Fumiko Tajima[1] and Aitaro Kato[2]

[1]*Department of Earth and Planetary Systems Science, Graduate School of Science, Hiroshima University,* 1-3-1 *Kagamiyama, Higashi Hiroshima City* 739-8526*, Japan. E-mail: re-ko-is-loving-it@hiroshima-u.ac.jp*
[2]*Earthquake Research Institute, University of Tokyo,* 1-1-1 *Yayoi, Bunkyo-ku, Tokyo* 113-0032*, Japan.*

Accepted 2008 November 6. Received 2008 October 5; in original form 2008 July 24

SUMMARY

The seismic velocity structure in and around the source area of the 2004 mid-Niigata earthquake, which featured complicated heterogeneities, was investigated by combining waveform modelling and traveltime tomography inversion using low-frequency ($0.05 \leq f \leq 0.2$ Hz) and high-frequency ($f \geq \sim 1$ Hz) data, respectively. On the footwall of the main shock that includes multiplanar faults, 3-D finite-difference waveform modelling using only a previously proposed tomography model was not sufficient to synthesize the observed waveforms in $0.05 \leq f \leq 0.2$ Hz at most stations. Thus, we derived a final 3-D model 3DM-28, examining body wave amplitudes, phases and traveltimes. The image produced by model 3DM-28 shows a clearer contrast between low- and high-velocities than that seen in the original tomography models due to the higher velocity on the footwall. This increase in velocity, particularly in the seismogenic zone, also indicates that short-wavelength low-velocity anomalies revealed in the revised tomography image may be more localized in the vicinity of the multiplanar faults than that shown in the original one. Moreover, the low-velocity anomaly zone within a depth range of 15–20 km beneath the seismogenic zone (lower crust) appears to be associated with the short-wavelength low velocity anomalies at shallower depths (upper crust). These characteristics may support the hypothesis of infiltration of pressurized fluids from the lower crust into the multiplanar fault system. The volumes or distributions of such fluids may be clarified by further examination of 'unsatisfactory fit waveforms' recorded at stations along the strikes of the major faults. We suggest that the clear velocity contrasts between the hangingwall and footwall and the upper crust and lower crust, including the effects of fluids, all seem to be essential characteristics of the seismogenic conditions in this earthquake sequence.

Key words: Earthquake dynamics; Body waves; Seismic tomography; Computational seismology; Wave scattering and diffraction; Wave propagation.

1 INTRODUCTION

The mid-Niigata prefecture earthquake occurred on 2004 October 23, approximately 30 km inland from the west coast of central Japan. This earthquake had a moment magnitude (M_W) of 6.6 and a reverse-fault mechanism with a strike of N32°E (Fig. 1). A large number of aftershocks, including six events with $M_W \geq 5.5$, were felt over a period of about 2 week in this earthquake sequence (Fig. 1b). The source parameters of the large events are summarized in Table 1. The distribution of aftershock hypocentres suggests the existence of at least three major faults (e.g. Aoki *et al*. 2005; Kato *et al*. 2005; Shibutani *et al*. 2005). As shown in Fig. 1(c), two parallel clusters of aftershock hypocentres dipping west-northwest correspond to faults of the main shock (E1) and the largest aftershock (M_W 6.3; E4), whereas that dipping east-southeast correspond to a conjugate fault causing the aftershock that occurred on October 27 (M_W 5.8; E5).

The Niigata district is located in the region of tectonic strain concentration along the Niigata–Kobe tectonic zone (Sagiya *et al*. 2000). The geological structure around the source region is composed of two parts; the hangingwall on the northwestern side and the footwall on the southeastern side of the main shock fault, which consist of a thick (≤6 km) Neogene sedimentary basin (Niigata Basin) and a basement of older rocks (virtually without a sedimentary cover), respectively (Takeuchi *et al.* 2004). Geological studies indicate that profound surface folding with a NNE–SSW fold axis

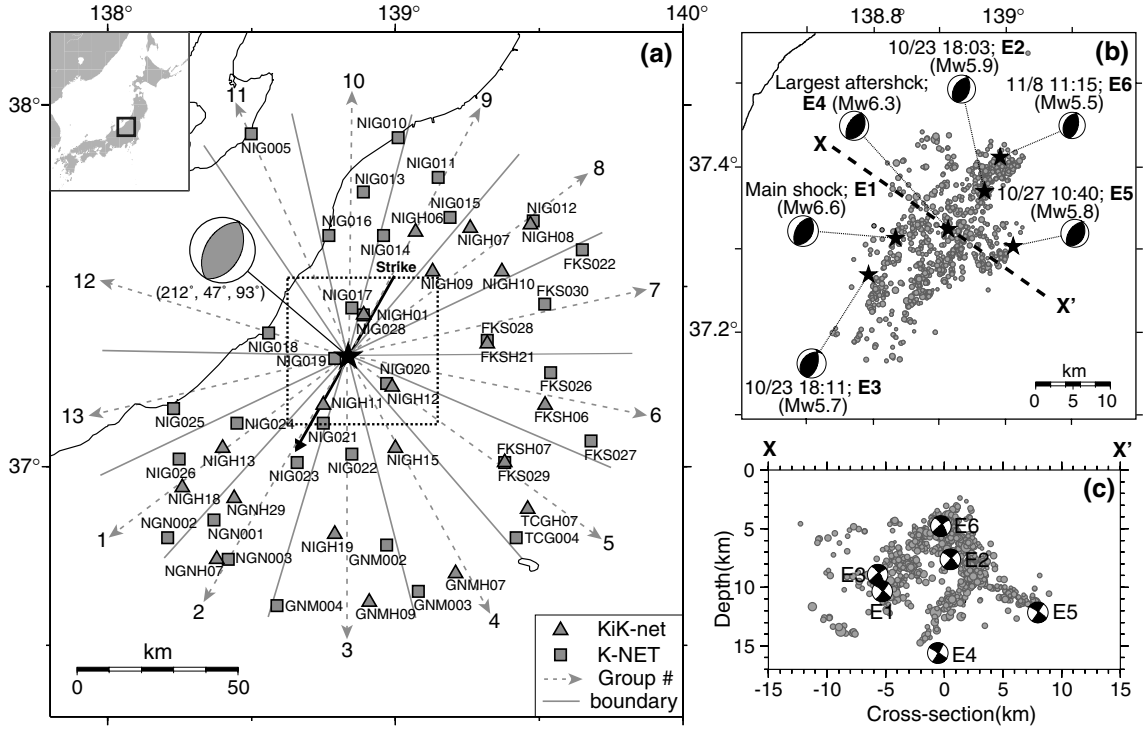

Figure 1. (a) Locations of the main shock of the 2004 mid-Niigata earthquake (star) with its focal mechanism, and 32 K-NET (squares) and 20 KiK-net (triangles) stations used in this study. Dashed lines with arrows denote the directions to divide the stations into 13 groups. Grey solid lines denote the boundaries between the groups. The number at each arrowhead denotes the group number (groups 1 to 13). The area indicated by the dotted inner box corresponds to the area shown in (b). (b) Map view of the epicentral distribution of six large events (stars), E1–E6, listed in Table 1, and 915 aftershocks (grey circles), relocated by Kato *et al*. (2006). Focal mechanisms are determined by the NIED F-net (Fukuyama *et al.* 1998). (c) Vertical cross-section with superimposed relocated hypocentres along line X (W35°N) –X′ (E35°S) shown in (b). The line is through the centre of the aftershock distribution and at right angles to the strike of the inferred main shock fault.

Table 1. Source parameters of the 2004 mid-Niigata prefecture earthquake sequence.

Event name	Origin time (JST)[a] (y/m/d, h:m:s)	Latitude[b] (deg)	Longitude[b] (deg)	Depth[b] (km)	Strike[a] (deg)	Dip[a] (deg)	Rake[a] (deg)	M_0[a] (Nm)	M_W[a]
E1 (Main shock)	2004/10/23,17:56:00	37.3113	138.8319	10.42	212	47	93	7.53×10^{18}	6.6
E2	2004/10/23,18:03:12	37.3682	138.9664	7.64	218	47	107	9.33×10^{17}	5.9
E3	2004/10/23,18:11:56	37.2672	138.7909	9.08	234	37	118	4.11×10^{17}	5.7
E4 (LA)	2004/10/23,18:34:05	37.3221	138.9111	15.71	221	59	94	2.93×10^{18}	6.3
E5 (27 October)	2004/10/27,10:40:50	37.3015	139.0097	12.14	18	32	73	6.34×10^{17}	5.8
E6	2004/11/08,11:15:58	37.4095	138.9900	4.81	209	38	103	2.24×10^{17}	5.5

[a]after the NIED F-net event catalogue.
[b]after the relocated catalogue by Kato *et al.* (2006).

has developed since 3.5 Ma due to compression within the sedimentary basin, following an extensional stage during the opening of the Japan Sea (Sato 1994).

Seismic local tomography models of traveltime inversions determined for the source area of this earthquake sequence indicate that the aftershocks along the main shock rupture zone are distributed around the boundary between high- and low-velocity zones, and parts of the hypocentres or fault planes are imaged as low-velocity anomaly zones. The velocity contrast extends to approximately 10 km in depth (e.g. Korenaga *et al.* 2005; Kato *et al.* 2006; Okada *et al.* 2006). However, the regions of high resolution in the tomography model are restricted to the region of concentrated aftershock hypocentres in an area of about 30 km^2 and up to a depth of about 15 km. Moreover, the quality of the *S*-wave velocity (V_S) model is lower than that of the *P*-wave one (V_P) because of the uncertainties in determining *S*-wave arrival times.

Broader examination of a tomography model for a 150 km^2 region of depth less than 50 km (Okada *et al*. 2006) shows large low-velocity anomalies beneath the hypocentral region. In this case, the anomalous low-velocity zones in the vicinity of the multiplanar faults revealed in the local tomography model cannot be seen because of the large grid intervals, set at 20 km horizontally and 8 km in depth. The multiplanar faults of the large events ($M_W \geq$ 5.5) with profuse aftershocks lie mainly on the footwall within a depth range of ∼3–15 km, and 15 km depth is the approximate base of the seismogenic zone. However, high-resolution examination around the base of the zone is difficult with the existing models. Therefore, we attempt to calculate waveforms using a 3-D structure based on the local tomography model. We then examine the velocity structure within the region that includes the seismogenic and non-seismogenic zones at a depth of ∼15 ± 5 km. With a similar approach using broad-band waveform modelling, global or regional

tomography models were evaluated to find variation of seismic velocity anomalies and mineral physics implications (e.g. Tajima & Grand 1998; Tajima *et al*. 1998; Tajima & Nakagawa 2006).

The seismic velocity models adopted control the numerical results of source process analysis and seismic wave simulation. The effects of structural heterogeneity around the source area as well as near the surface are essential to synthesize waveforms in terms of amplitudes and phases. Such effects seem to be particularly apparent for this earthquake sequence since the source area includes the velocity contrast extending over the hypocentral depth of ∼10 km. Waveform inversions for source processes (e.g. Hikima & Koketsu 2005; Honda *et al*. 2005) and seismic wave simulations (e.g. Furumura & Hayakawa 2007) were performed for this earthquake sequence, but the effects of structural heterogeneity near the source area are not significantly covered in those studies.

In this study, we construct a 3-D structure around the source area of the 2004 mid-Niigata earthquake using a finite-difference (FD) method. The 3-D velocity model is investigated by combining a revised tomography model and multiple 1-D models. In particular, we focus on the region in and beneath the heterogeneous seismogenic zone of ∼3–20 km in depth to investigate the physical mechanisms or seismogenic conditions around the source area.

2 1-D WAVEFORM MODELLING

2.1 Method and data

We first carry out forward modelling using a 1-D frequency–wavenumber (1D-FK) code of Saikia (1994) to examine the basic structural variation around the source area and then incorporate the derived 1-D models in constructing of the 3-D model. Fig. 1(a) shows the locations of the stations with the main shock epicentre. We synthesize the velocity (the integrated acceleration) waveforms of the main shock, which are recorded at 52 stations located within 80 km from the main shock epicentre. These stations are in two nationwide accelerometer networks, the Kyoshin Network (K-NET) and the Kiban Kyoshin network (KiK-net), maintained by the National Research Institute for Earth Science and Disaster Prevention (NIED).

The sets of three-component, strong-motion seismographs of the K-NET stations are ground surface located, and those of the KiK-net stations are located on the surface and within boreholes. Ideally, it is better to use only the borehole KiK-net stations, as the effects of amplification due to scattering near the surface is reduced (see Hayashida & Tajima 2007). However, as shown in Fig. 1(a), there are few KiK-net stations on the northwestern side of the main shock epicentre. We then compared the amplification between the ground surface and borehole stations, with the different frequency bands (Fig. A1). Based on the result, we adopt the velocity waveforms recorded at the K-NET and borehole KiK-net stations, excluding the surface KiK-net stations, that are bandpass-filtered within the frequency (f) range of 0.05–0.2 Hz, because of the minimal effects of amplification. We also checked how the first arrival P-waves sample the different velocity structures (Fig. A2). We made sure that the rays strongly sample the structure between ∼3 and 20 km in depth. Thus, we can examine the velocity structure within a ∼40 km horizontal distance from the epicentre and between ∼3 and 20 km in depth, using the velocity waveforms in $0.05 \leq f \leq 0.2$ Hz.

As shown by dashed lines and arrows in Fig. 1(a), the stations are grouped in 13 azimuthal ranges according to the locations surrounding the main shock epicentre (groups 1 to 13) for the detailed waveform modelling. The stations in each group are in the same direction but have different hypocentral distance. For each group, we construct a layered velocity structure that explains the data at the stations, by checking cross-correlations between the observed and synthetic waveforms. We use the source parameters of the main shock summarized in Table 1 (after the event catalogues of Kato *et al*. 2006 and the NIED F-net) and a source time function (STF) with ∼8 s duration after the inversion result, using the teleseismic and near-field body waves by Yagi (2005). A Poisson's body was assumed to compute V_S ($V_S = V_P/1.73$). The structures for density (ρ) and Q of P and S waves (Q_P, Q_S) are summarized in Table 2.

Table 2. Layered structure of density and attenuation.

Depth[a] (km)	Thickness (km)	ρ (gm cm^{-3})	Q_P	Q_S
0.0	0.5	2.0	100	50
0.5	1.0	2.3	300	150
1.5	3.0	2.5	500	250
4.5	10.5	2.6	700	350
15.0	15.0	2.7	800	400
30.0	40.0	2.8	1000	500
70.0	–	3.0	2000	1000

[a]Depth to the top of the layer.

2.2 Derived multiple models

We derived 14-layered structures (models 1DM-1a, -1b, -2a, -2b, -3 to -9, -10a, -10b and -12) from the forward modelling as described above. The numbers used for the model identifications and groups do not always correspond to each other because there are two models in each group (distinguished as a and b) and redundant models in two groups. The data recorded at the stations on the footwall could be synthesized based on the individual 1D-FK models adequately, but the later arriving waves at stations on the hangingwall could not be synthesized using the models. For example, consider the results of stations in Group 1 on the hangingwall (Fig. 2a) and in Group 4 on the footwall (Fig. 2b). Here we define the hangingwall and footwall as relative to the rupture of the main shock fault dipping west-northwest (see Fig. 1b).

At the stations in Group 1 distributed on the southwestern side of the main shock epicentre (see Fig. 1), we derived model 1DM-1a that has a sudden increase of velocities at depth of ∼7.5 km accompanied by a low-velocity layer from ∼12 to 16 km depth (pink lines in Fig. 2a). The waves in the group sampled the structure of the hangingwall. As shown in Fig. 2(a), fits between the data and the synthetics with model 1DM-1a (pink lines) are better than those with 1-D models used by Kato *et al*. (2006) and Honda *et al*. (2005) in the arrival of P and S waves. But, the fits in the later arriving waves are not satisfactory. In addition, at station NIG024 with the relatively short epicentral distance (Δ) ∼40 km, the data could not be synthesized well using model 1DM-1a. Most rays have upward paths in the structure from the source (10 km depth) to the stations within $\Delta \leq$ ∼40 km (see Fig. A2). We then adopted model 1DM-1b that had a low velocity layer within the depth $\leq$ 12 km. The low-velocity layers imposed in our models for Group 1 stations on the hangingwall (also those of groups 12 and 13) seem to reflect effects that cannot be explained by the 1-D structure, with there possibly being a strong influence from the sedimentary basin.

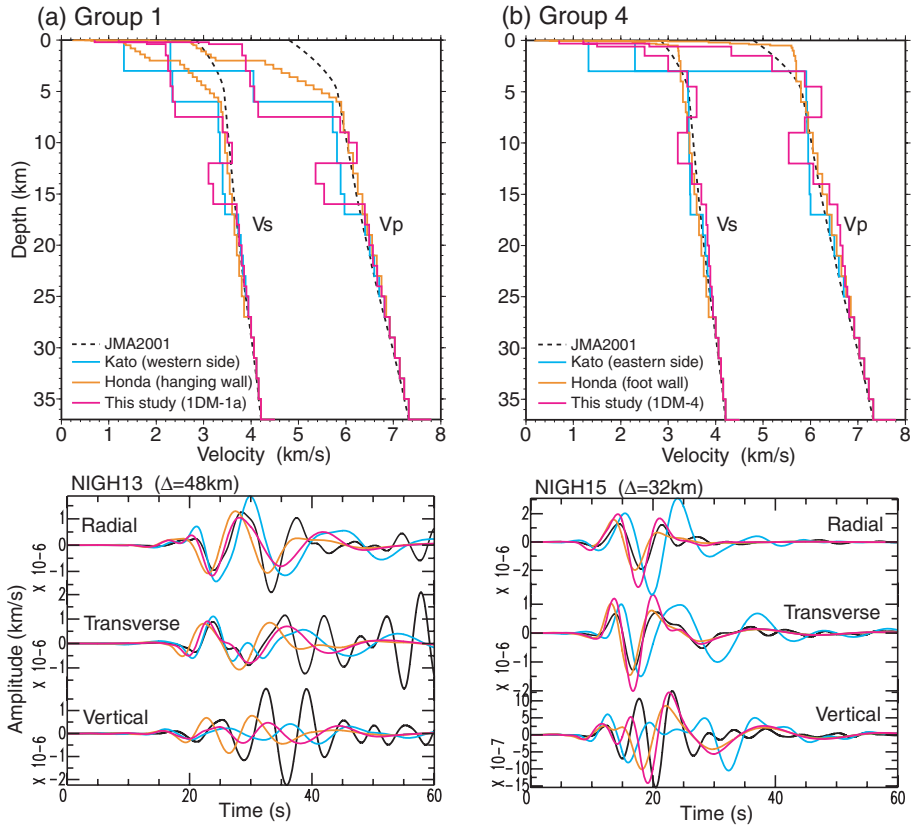

Figure 2. Comparison between 1-D velocity models derived in this and other studies, and fits between three-component, bandpass-filtered ($0.05 \leq f \leq 0.2$ Hz) velocity data and frequency–wavenumber (FK) synthetic waveforms, for the main shock. (a) (Top) Velocity models of P (V_P) and S (V_S) waves from 0 to 37 km depth. Black dotted, solid light blue, orange and pink lines, respectively, denote the model JMA2001 derived by Ueno *et al.* (2002), the initial model on western side used by Kato *et al.* (2006), the hangingwall model used by Honda *et al.* (2005) and model 1DM-1a of Group 1 derived in this study. (Bottom) Example of comparison between the data (black lines) and the synthetic waveforms (coloured lines) at NIGH13 (the epicentral distance $\Delta = 47.9$ km) in Group 1. The coloured lines correspond to the colour of each model in (top). Top, middle and bottom traces in each graph correspond to radial, transverse and vertical components, respectively. (b) Same as (a), but (Top) black dotted, solid light blue, orange and pink lines, respectively, denote model JMA2001, the initial model on the eastern side used by Kato *et al*. (2006), the footwall model used by Honda *et al*. (2005) and model 1DM-4 of Group 4 derived in this study. (Bottom) The station is NIGH15 ($\Delta = 31.7$ km) in Group 4.

At the stations in Group 4 that are distributed on the south-southeastern side of the main shock epicentre (see Fig. 1), we could well synthesize the observed waveforms using model 1DM-4 with a low-velocity layer near the hypocentre ∼10 km (pink lines in Fig. 2b). The waves sampled the structure of the footwall. Most of the data in Group 4 could be synthesized using the model for the footwall used by Honda *et al*. (2005), which did not have the low-velocity layer (orange lines in Fig. 2b). However, at station NIGH15 (Δ ∼31 km), model 1DM-4 explained the data better than the model used in Honda *et al*. (2005), especially in fits between the data and the synthetics from ∼10 to 15 s in the vertical component (see the third trace in Fig. 2b, bottom). The *P*-wave first arrival signal observed at station with Δ ∼31 km reaches the deepest point and well reflects the structure near the main shock hypocentre ∼10 km depth. We thus found that the agreement was improved when the low-velocity layer near the 10 km depth was added to such models as 1DM-4. Models for groups 3 to 8 located on the footwall (models 1DM-3, -4, -5, -6, -7 and -8) had different structures around the source depth from each other even though fits between the observed and synthetic waveforms, including those of Group 4, were also good.

The stations in groups 2, 9, and 10 are located in the vicinity of the boundary between the hanging and footwalls, that is, along the strikes of large events ($M_W \geq 5.5$). At the stations, there were both high- and low-fits between the data and the synthetics (models 1DM-2a, -2b, -9, -10a and -10b). From these results, the individual 1D-FK models seem to be valid for the footwall stations, but the unified 3-D approach is necessary to explain the structure of the sedimentary basin on the hangingwall and the complex lateral heterogeneities on the footwall and the boundary.

Herein we compare the structure between the hybrid 2-D model visualized using the multiple 1D-FK models and the vertical cross-section of the 3-D model derived from the tomography inversion by Kato *et al*. (2006) (Figs 3a and b). The hybrid 2-D profile at right angle to the strike of the main shock shown in top of Fig. 3(a) is a combination of 1-D models 1DM-3 and 1DM-5b in Group 5 and model 1DM-12 in Group 12. The velocity contrast along this vertical cross-section is similar to that in the tomography model (Fig. 3b). Likewise, the 2-D profile, which is parallel to the strike (Fig. 3a, bottom), consists of a combination of models 1DM-2a and 1DM-2b for Group 2 and model 1DM-9 for Group 9. This profile does not show a clear contrast between high and low velocities in the upper layers shallower than 10 km (Figs 3a, top, and b). The profiles of the sedimentary basin reported by the Niigata prefecture (2000) and Takeuchi *et al*. (2004) are drawn with black lines to make a comparison with the 2-D velocity profile in Fig. 3(a).

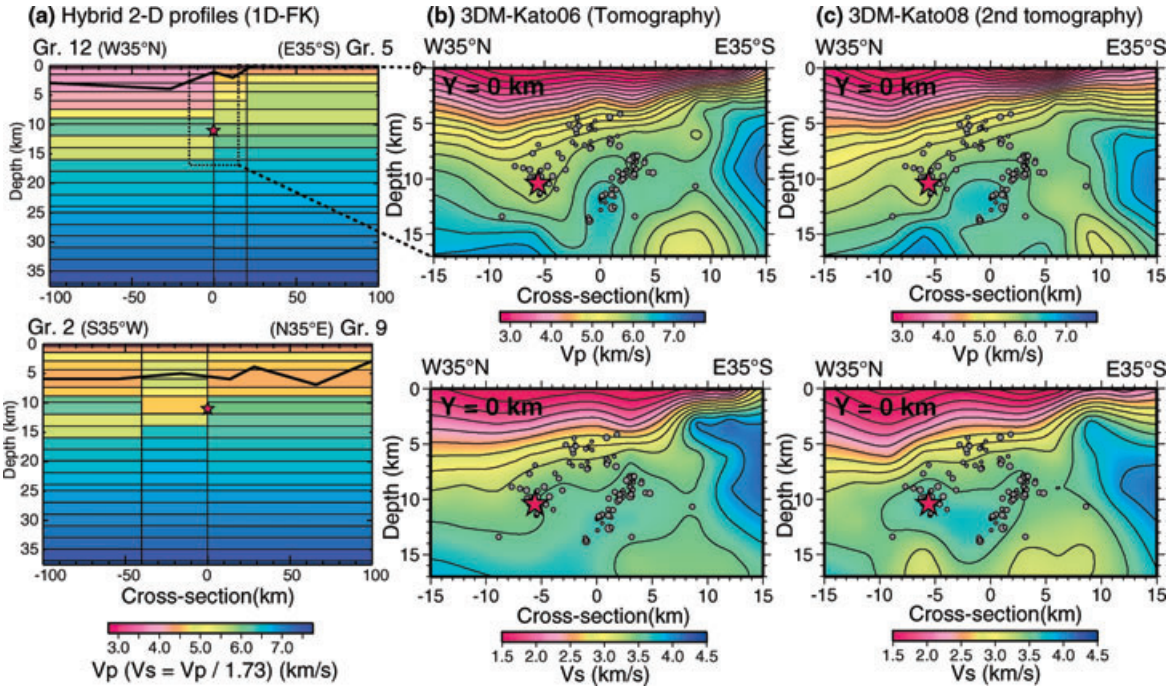

Figure 3. Comparisons between vertical cross-sections based on the 1D-FK and 3-D tomography models. (a) Hybrid 2-D profiles visualized by multiple 1D-FK models ($V_P = 1.73V_S$) with the profile of the sedimentary basin based on geological studies (black solid lines). Top and bottom diagrams are vertical cross-sections that cross at right angles to the strike of the main shock, along a line which links Group 12 (W 35° N) and Group 5 (E 35° E), and parallel to the strike, along a line which links Group 2 (S 35° W) and Group 9 (N 35° E), respectively. The area indicated by the dotted inner box corresponds to the area shown in the top of (b). (b) Cross-sections of areas of high-resolution (~30 × 15 km) in model 3DM-Kato06 by Kato *et al.* (2006) along the line from W 35° N to E 35° E of $y = 0$ km shown on the map view in Fig. 6(a) that crosses at right angles to the strike. Top and bottom diagrams are V_P and V_S models with superimposed relocated aftershocks distributed within ± 1.5 km from the section. The contour line interval is 0.25 kms^{-1}. (c) Same as (b), but cross-sections of model 3DM-Kato08 derived from the second tomography inversion using more data and a hybrid 3-D initial model based on multiple 1D-FK structures.

3 WAVEFORM SYNTHESIS BASED ON EXISTING TOMOGRAPHY IMAGES

3.1 3-D velocity structure constructed from a tomography model

We produce a 3-D waveform synthesis using model 3DM-Kato06, based on the local tomography model derived by Kato *et al*. (2006), to examine how much the observed waveforms are synthesized by the existing model. We use the elastic FD code, E3D, by Larsen & Schultz (1995) for the waveform calculation. As shown in Fig. 4(a), we employ a calculation volume of 200 × 200 × 100 km that has grid intervals of 0.3 km, a dimension from −100 to +100 km for the X (N 125° E) and Y (N 35° E) axes and a depth from 0 to 100 km for the Z axis. The origin, $(x, y, z) = (0, 0, 0)$, is located in the centre of the source area, as in the tomography model of Kato *et al*. (2006). The hypocentre of the main shock is thus set at $(x, y, z) = (-5.53, -0.32, 10.41)$ km.

The grid nodes of the tomography model are located at −300, −30, −18, −12, −9, −6, −3, 0, 3, 6, 9, 12, 18, 30 and 300 km on the X axis; −300, −30, −24, −18, −15, −12, −9, −6, −3, 0, 3, 6, 9, 12, 15, 18, 24, 30 and 300 km on the Y axis and –150, 0, 3, 6, 9, 12, 15, 20 and 300 km on the Z axis (see Kato *et al*. 2006). V_P and V_S set on the grid nodes in the tomography model are interpolated to correspond to the 3D-FD model. From the results of the checkerboard resolution test of Kato *et al*. (2006), the area of high resolution in the tomography model is from approximately −15 to +15 km for the X axis and from −12 to +18 km for the Y axis (30 km^2) and has a depth range of 1.5–15 km on the Z axis. The 1-D model JMA2001 (Ueno *et al.* 2002) is inserted into the depth of over +20 km in the FD model because the grid nodes for the tomography reach depths of 20–300 km. This replacement seems to be appropriate since a small horizontal heterogeneity below 20 km depth was confirmed in previous 1D-FK analyses. Thus, the structure of model 3DM-Kato06 has complex heterogeneities including the difference between the hangingwall and footwall around the source area. In the model, the waveforms of $f \leq 0.44$ Hz can be stably calculated using a minimum velocity, $V_S = 1.328$ kms^{-1}, and an arbitrary 10 gridpoints for the shortest usable wavelength in the model. We employ velocity waveforms in $0.05 \leq f \leq 0.2$ Hz that are recorded at 52 K-NET and KiK-net stations, as with the 1D-FK analysis.

We use the same seismic source parameters for the main shock (Table 1), ρ, Q_P, Q_S (Table 2) and STF as for the 1D-FK analysis and a reference frequency of 1 Hz. For the source parameters, the hypocentral locations were relocated using a double-difference (DD) tomography method that determines the hypocentres as well as the velocity structure simultaneously (see Kato *et al.* 2006). The uncertainties of the relocated hypocentres of the main shock, the largest aftershock and the aftershock on October 27 are ~ ±0.6, ±0.7 and ±0.3 km in the horizontal direction and ~ ±2.0, ±1.4 and ±0.6 km in the vertical direction, respectively (see fig. 2 in Kato *et al*. 2005). Thus, the source locations were determined consistently with the local tomography model. The focal mechanism and seismic moment (M_0) are employed from the event catalogues of NIED F-net (Fukuyama *et al*. 1998). These parameters are more or less similar to those used by other studies of source inversion (e.g. Hikima & Koketsu 2005; Honda *et al*. 2005). Therefore, we carry

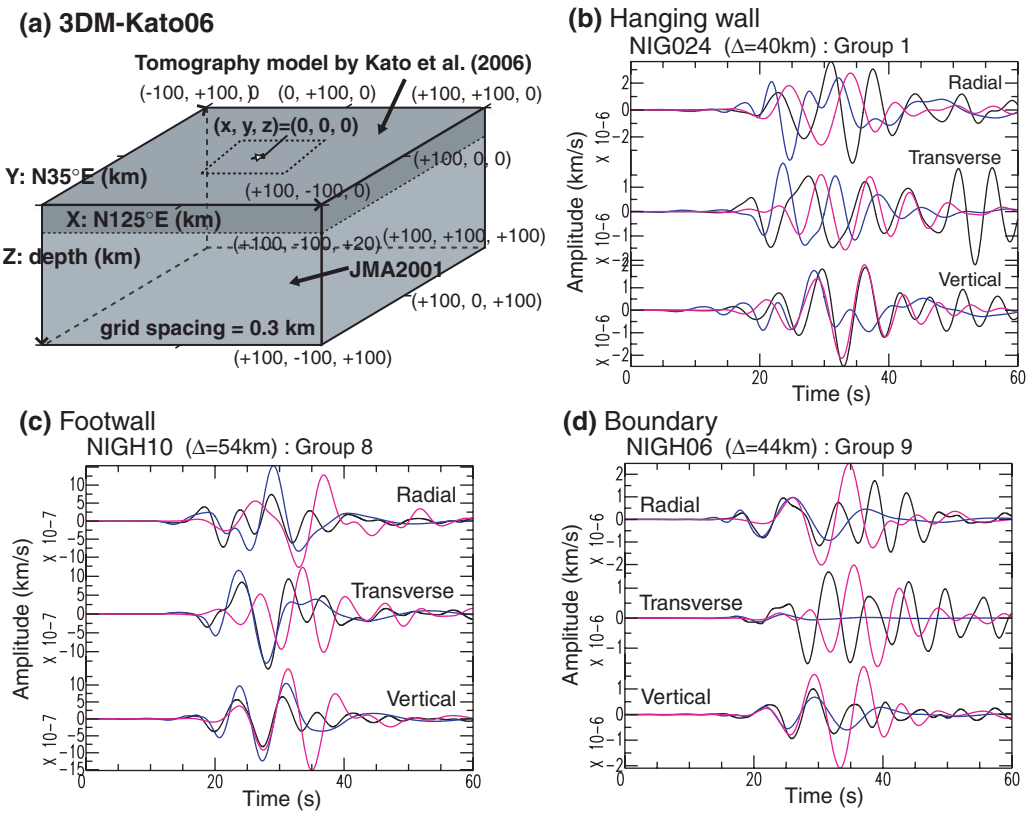

Figure 4. Examples of the comparison between three-component, bandpass-filtered ($0.05 \leq f \leq 0.2$ Hz) velocity data (black lines) and synthetic waveforms calculated using the FK and finite-difference (FD) codes with each 1-D model (blue lines) and model 3DM-Kato06 based on the tomography model by Kato *et al*. (2006) (pink lines), respectively, for the main shock. (a) Geometry of the 3-D model 3DM-Kato06 that has the entire calculation volume of 200 × 200 × 100 km with a dimension from −100 to +100 km for the X (N 125° E) and Y (N 35° E) axes and depth from 0 to 100 km for the Z axis, and the grid spacing of 0.3 km^3. (b) Comparison between the data and the synthetics at station NIG024 on the hangingwall. The station ID, Δ and group number are given in the upper left-hand side of each diagram. Top, middle and bottom traces in each graph correspond to radial, transverse and vertical components, respectively. (c) and (d) same as (b) but at station NIGH10 on the footwall and at station NIGH06 near the boundary between the hanging and footwalls.

out the 3D-FD waveform modelling by assuming a point source that has minimal ambiguities due to a trade-off between the source and the heterogeneous structure in this earthquake sequence.

3.2 Comparison between observed and synthetic waveforms

We obtained relatively stable 3D-FD synthetic waveforms with the 3DM-Kato06 model, including the high-resolution heterogeneous structures around the source area derived from the local tomography. Especially, the vertical component data, including those of later arriving waves recorded at stations on the hangingwall, could be synthesized using the model (pink lines in Fig. 4b). However, the synthetic waveforms based on the model are in poor agreement with the observed waveforms at stations on the footwall because the synthetics had some phase delays and overly large amplitudes, particularly for the later arriving waves (pink lines in Fig. 4c). This tendency is strong for the synthetics at stations south to southeast of the main shock epicentre (groups 3–5). The misfit on the footwall should be improved to examine complex lateral heterogeneity, including the multiplanar faults. The result derived from the waveform modelling using the existing tomography model is in contrast with that from the 1D-FK analysis and means that the relatively large structural effects of low-velocity for the sedimentary basin can be explained using only the tomography model (Figs 4b and c).

Moreover, the synthetics have both high- and low-fits with the data at stations in groups 2, 9 and 10, that is, the boundary between the hanging and footwalls, as in the 1D-FK models (Fig. 4d). The zone is presumed to have a complicated structure along the basin boundary or strikes of the major faults and requires a more detailed examination. From these results, we made sure that the 3-D structure based only on the traveltime tomography model are not sufficient to synthesize the data recorded at most stations, especially those on the footwall and the boundary between the hanging and footwalls.

4 IMPROVEMENT OF THE 3-D VELOCITY STRUCTURE

4.1 Second tomography inversion and construction of an initial model

In the previous two sections, we found that the results of the waveform modelling with the multiple 1D-FK models derived here and model 3DM-Kato06 based on the tomography were complementary to each other between the hangingwall and footwall of the main fault. To combine the characteristics of the two models, we carried out a DD tomography inversion after Zhang & Thurber (2003) using a hybrid 3-D initial model based on 14 1D-FK models and more arrival-time data with better-covered ray paths of Kato *et al*. (2007). The method used was after Kato *et al*. (2006). We then applied the

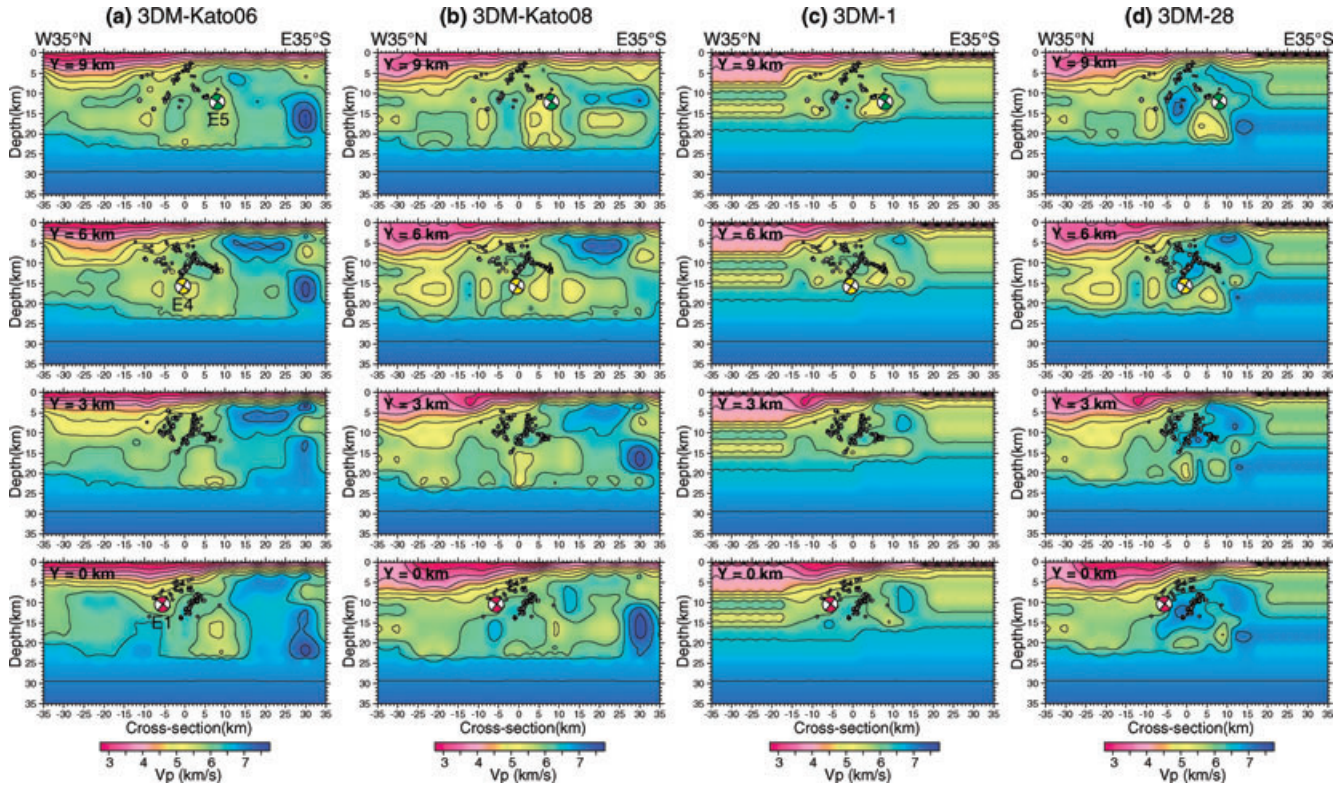

Figure 5. Comparison of images of 3-D V_P models. Top, second, third and bottom diagrams, respectively, denote the vertical cross-sections along lines from W35°N to E35°E at positions of $y = 9$, 6, 3 and 0 km shown on the map view in Fig. 6(a) that cross at right angles to the strike. The contour line interval is 0.5 km s^{-1}. (a) Model 3DM-Kato06 based on tomography model by Kato *et al*. (2006). (b) Model 3DM-Kato08 derived from second tomography inversion using more data and a hybrid 3-D initial model based on multiple 1D-FK structures. (c) 3-D initial model 3DM-1 shown geometrically Fig. 6(a). (d) The final improved model 3DM-28 shown geometrically in Fig. 6(e).

3D-FD waveform modelling, as we did for model 3DM-Kato06, to model 3DM-Kato08 based on the new tomography model derived from the second traveltime inversion.

Figs 3(b) and (c) show the vertical cross-sections, at a right angle to the strike of the main shock fault within the high-resolution area of ∼30 × 15 km, for models 3DM-Kato06 and 3DM-Kato08. Figs 5(a) and (b) also show the cross-sections for the two models within broader areas (∼70 × 35 km) than those of Figs 3(b) and (c). The basic images in the area of high resolution for models 3DM-Kato06 (Fig. 3a) and 3DM-Kato08 (Fig. 3b) are similar to each other within the grid nodes (≥3 km). Moreover, the low-velocity anomalies from 10 to 20 km depth in model 3DM-Kato08 (Fig. 5b) are clearer than those of model 3DM-Kato06 (Fig. 5a). The differences may suggest the low model resolutions of the tomography models since each tomography image should be similar in the high-resolution area even if the initial models or the data are different.

The difference between images corresponding to the two tomography models is predictably large in the areas with low model resolution. This may not pose a problem when we interpret only the areas of high resolution. However, the image differences affect the waveform modelling, particularly for structure at a depth between ∼10 and 20 km. The structure is important to synthesize waveforms for the major events and interpret the seismogenic conditions. We adopt model 3DM-Kato08 (Figs 3c and 5b) to improve the 3D-FD structure since the agreement between the data and the synthetics with model 3DM-Kato08 is improved for stations on the footwall, when compared with those of model 3DM-Kato06.

Here we construct an initial 3-D model 3DM-1 based on the 3DM-Kato08 framework and a combination of multiple 1D-FK models (Fig. 6a). In model 3DM-1, an area of high resolution in model 3DM-Kato08, with a volume of 30 × 30 × 15, $-15 \le x \le +15$, $-12 \le y \le +18$ and $0 \le z \le +15$ km, is inserted into the centre of a hybrid 3-D model made from the combination of 14 1D-FK structures set to the entire volume of 200 × 200 × 100 km. Starting from model 3DM-1, we test various models with different velocity conditions to improve the 3-D structure, considering the effective region of within a ∼40 km horizontal distance from the epicentre and between ∼3 and 20 km in depth (see Fig. A2). We adopt the same source parameters of the main shock, ρ, Q_P, Q_S, STF and reference frequency as in previous FD analyses with models 3DM-Kato06 and 3DM-Kato08. We also employ velocity waveforms in $0.05 \le f \le 0.2$ Hz.

4.2 Improvement procedure

We carried out waveform modelling with the initial 3-D model 3DM-1 (Fig. 6a) using the FD method similar to that of model 3DM-Kato08. The data recorded at stations on the hangingwall (groups 1, 2, 9–13) could not be synthesized using model 3DM-1 adequately. On the other hand, these data could be synthesized based on model 3DM-Kato08, as for model 3DM-Kato06. We thus made model 3DM-6 that has a structure of model 3DM-Kato08 on the entire hangingwall in model 3DM-1, $-100 \le x \le -5.5$, $-100 \le y \le +100$, and $0 \le z \le +15$ km (Fig. 6b). As a result, the agreement between the data and the synthetics with model 3DM-6 for the stations on the hangingwall was improved (see comparison between fourth and fifth traces in Fig. 7a, top).

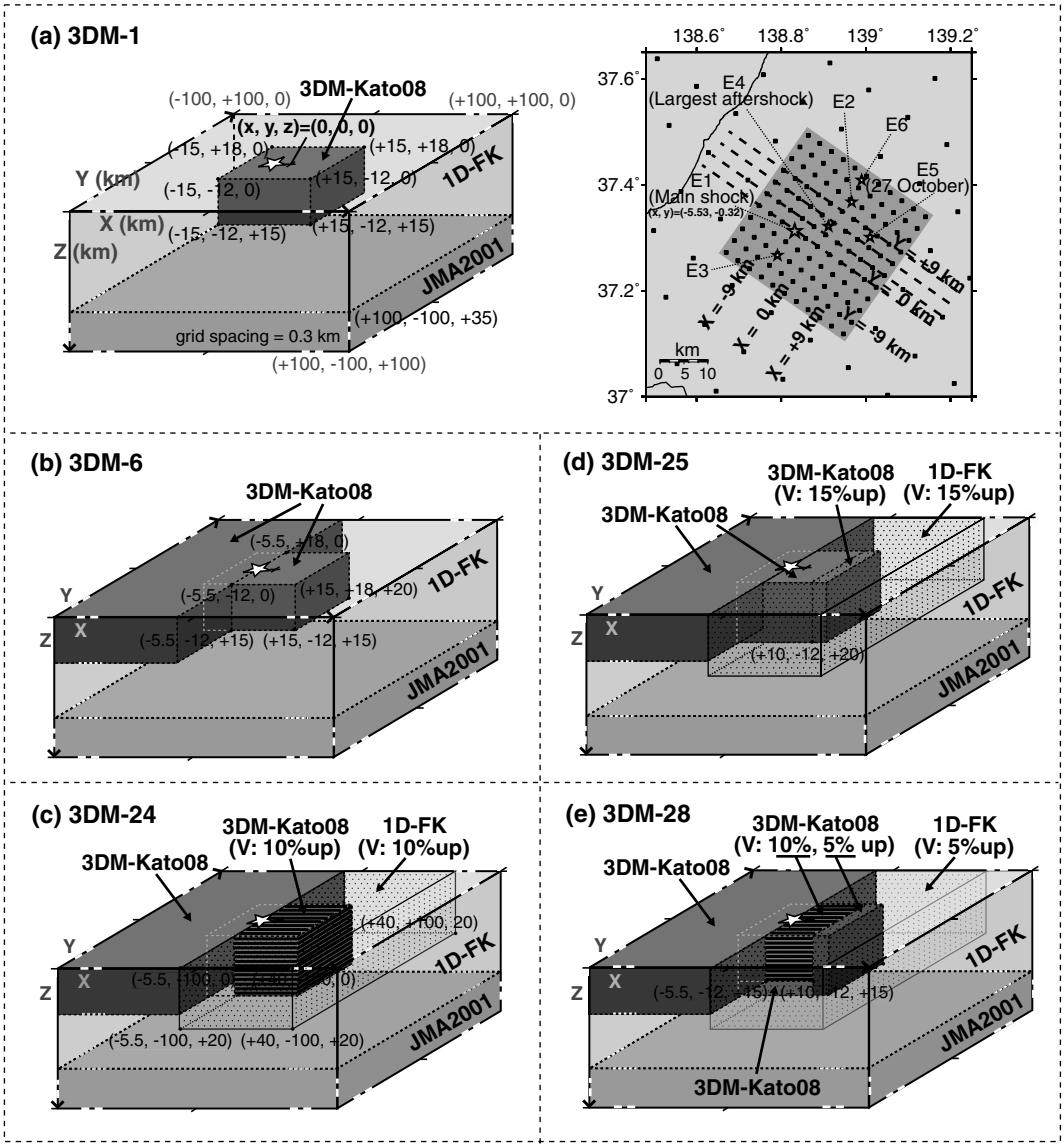

Figure 6. Geometry of 3-D models in the process of improvement from the initial model to the best model. (a) (Left-hand panel) 3-D initial model 3DM-1. (Right-hand panel) Expansion of the map view of dark grey inner box in the diagram on the left-hand side that shows grids used in model 3DM-Kato08 (crosses) and four horizontal lines (dashed lines) for the vertical cross-sections in Fig. 5. (b) Model 3DM-6, which has the inserted model 3DM-Kato08 in the entire hangingwall of model 3DM-1. (c) Model 3DM-24, which has 10 per cent faster V_P and V_S structures on a part of the footwall, $-5.5 \le x \le +40$ km, $-100 \le y \le +100$ km and $0 \le z \le +20$ km, than model 3DM-6. (d) Model 3DM-25, which has 15 per cent faster V_P and V_S structures in model 3DM-24 accepting the original structure of a portion of model 3DM-Kato08 in the seismogenic zone measuring $-5.5 \le x \le +10$, $-12 \le y \le +18$ and $0 \le z \le +20$ km. (e) The final improved model 3DM-28, which has 5 per cent faster V_P and V_S structures in the region of $-5.5 \le x \le +40$, $100 \le y \le +100$ and $0 \le z \le +20$ km and consists of model 3DM-Kato08 and multiple 1D-FK models; however, it is 10 per cent faster in the seismogenic zone of a portion of model 3DM-Kato08 for the footwall, $-5.5 \le x \le +10$, $-12 \le y \le +18$ and $0 \le z \le +15$ km, plus the original model 3DM-Kato08 in the area beneath the seismogenic zone on the footwall, $-5.5 \le x \le +10$, $-12 \le y \le +18$ and $+15 \le z \le +20$ km, and the entire hangingwall, $-100 \le x \le -5.5$, $-100 \le y \le +100$ and $0 \le z \le +15$ km.

Furthermore, the fits between the data and the synthetics with model 3DM-1 for the footwall (groups 3 to 8) were also not satisfactory as those with models 3DM-Kato06 and 3DM-Kato08. Footwall heterogeneities within the depth range of ∼3–15 km were presumed from the previous 1D-FK and tomography analyses. The poor agreement for the footwall, that is, the synthetics with some phase delays and too large amplitudes, might be affected by the lateral heterogeneities that have the low-velocity anomaly zones around the seismogaenic zone, including the multiplanar faults (see Figs 5a–c). We judged that some velocity increases around the seismogaenic zone were necessary to improve the agreement of waveforms on the footwall.

We examined 24 models (models 3DM-3, -4, and -7 to -28) with velocity increases ranging from 5 to 15 per cent on the footwall, $-5.5 \le x \le +100$, $-100 \le y \le +100$, and $0 \le z \le +20$, by checking cross-correlations between the data and the synthetics. In the individual model, we also examined effects of the spatial distribution given the velocity increase, ranging from 5 to 20 km interval.

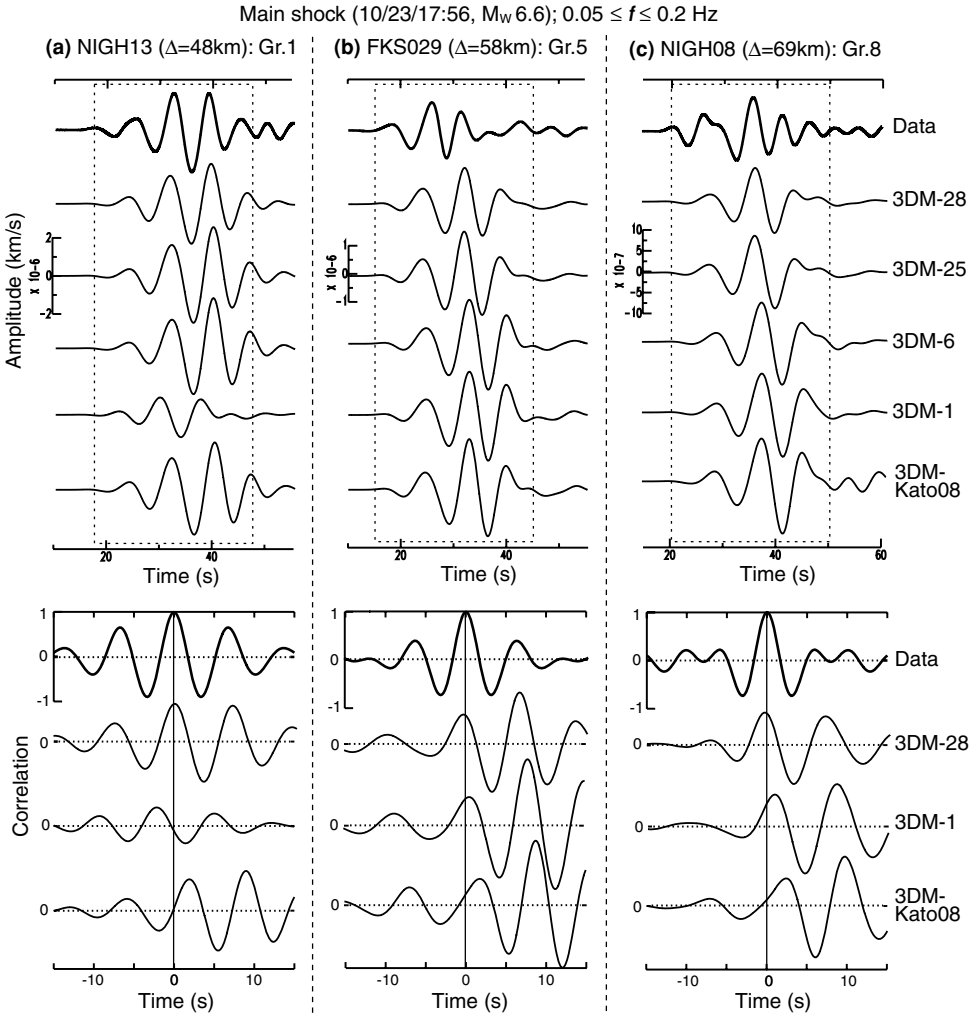

Figure 7. Examples of the fits between vertical component, bandpass-filtered ($0.05 \leq f \leq 0.2$ Hz) velocity data and 3D-FD synthetic waveforms at stations (a) NIGH13 ($\Delta = 48$ km. Group 1), (b) FKS029 ($\Delta = 58$ km. Group 5) and (c) NIGH08 ($\Delta = 69$ km. Group 8) for the main shock in the process of improvement. (Top) Comparisons between the data (first trace) and the synthetics (second, third, fourth, fifth and sixth traces are synthetics calculated using models 3DM-28, 3DM-6, 3DM-3, 3DM-1 and 3DM-Kato08, respectively). (Bottom) Autocorrelations of the observed waveform (first trace) and correlations between observed and synthetic waveforms (second, third and fourth traces are synthetics calculated using models 3DM-28, 3DM-1 and 3DM-Kato08, respectively).

As described above, we carefully investigated the velocity structure within a ∼40 km horizontal distance from the epicentre of the main shock and between ∼3 and 20 km in depth, using velocity waveforms at an epicentral distance of $\Delta \leq 80$ km and the frequency band of $0.05 \leq f \leq 0.2$ Hz, which have the minimal effects of amplification near the ground surface (see Figs A1 and A2). For example, we tested model 3DM-24, which has 10 per cent faster V_P and V_S structures on a part of the footwall than model 3DM-6 (Fig. 6c). Furthermore, we considered model 3DM-25 with 15 per cent faster V_P and V_S structures in model 3DM-24, accepting the unchanged structure of a portion of the new tomography model 3DM-Kato08 in a seismogenic zone (Fig. 6d). Based on these results, we found that the velocity increase around the seismogenic zone is valid, but that outside the source area, as in the 3DM-25 model (Fig. 6d), were invalid for improvement of the agreement for the phases and the amplitudes. The invalid tendency was particularly noteworthy at the stations with $\Delta \geq$ ∼60 km, the phases came early but the amplitudes remain too large in the synthetic waveforms when a sudden velocity increase was permitted outside the source area (see third traces in Figs 7b and c, top).

As shown in Fig. 6(e), we finally adopted model 3DM-28 as the final improved 3-D model, which has 5 per cent faster V_P and V_S structures in the region of $-5.5 \leq x \leq +40$, $100 \leq y \leq +100$ and $0 \leq z \leq +20$ km and consists of model 3DM-Kato08 and multiple 1D-FK models; however, it is 10 per cent faster in the seismogenic zone of a portion of model 3DM-Kato08 for the footwall, plus the original model 3DM-Kato08 in the area beneath the seismogenic zone ($+15 \leq z \leq +20$ km) on the footwall and the entire hangingwall. Fig. 7 shows the comparison of fits between the data and the synthetics calculated using the five models 3DM-Kato08, 3DM-1, 3DM-3, 3DM-6 and 3DM-28 improved step by step with the correlations between the data and the synthetics in models 3DM-28, 3DM-1 and 3DM-Kato08. These figures indicate that the data at stations on both the hangingwall (Fig. 7a) and footwall (Figs 7b and c) could acceptably synthesized based on model 3DM-28. Fig. 8 also shows the comparison of fits between the data and the synthetics with the three models 3DM-28, 1D-FK (models 1DM-1a to -12) and 3DM-Kato06. As shown in these figures, the agreement between the data and the synthetics with model 3DM-28 is satisfactory in all the groups.

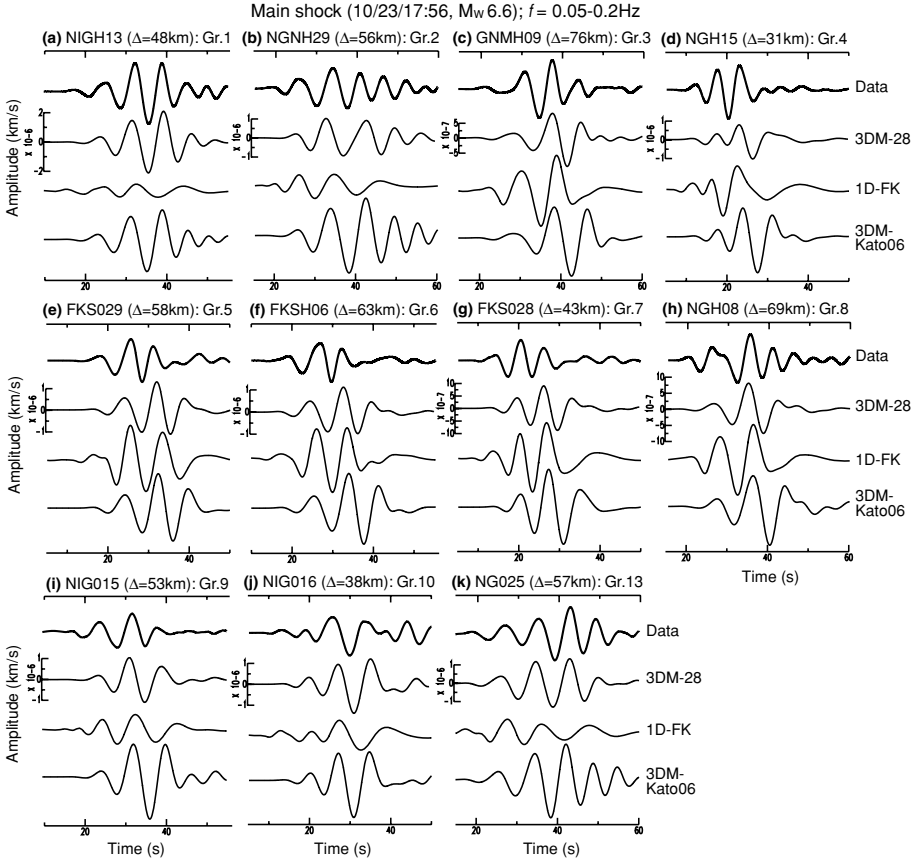

Figure 8. Examples of comparison between vertical component, bandpass-filtered ($0.05 \leq f \leq 0.2$ Hz) velocity data (firth trace) and synthetic waveforms calculated using model 3DM-28 (second trace), each 1D-FK model (third trace) and model 3DM-Kato06 (fourth trace), at stations in each group. The station ID, Δ and group number are given in the upper left-hand side of each diagram. Model 3DM-28 well synthesizes the observed waveforms for most groups.

4.3 Problems to be resolved of model 3DM-28

As described in the previous section, the improved model 3DM-28 can explain the data for the main shock at most stations. However, it has problems remaining to be resolved. First, we found 'unsatisfactory fit waveforms' recorded at several stations near the boundary between the hanging and footwalls along the strikes of the major events (see Fig. 9a, top). These waveforms seem to be generated as beating (interference) and could not be synthesized based on model 3DM-28 as shown in Fig. 9(a). Similar patterns also appeared in the observed waveforms for the largest aftershock and event on October 27 at stations along the strike, but the signal characteristics vary for the stations and each event. The anomalous waveforms may be related to anomalous structures in the vicinity of the fault rupture of the major events (the detail is discussed in the following section).

Second, the vertical component data synthesized using model 3DM-28 are adequate, but those of the horizontal components tend to become unstable. At a number of stations, the horizontal waveforms show phase shifts between the radial and transversal components (Fig. 9b). This may be related to shear wave splitting affected by fluid content, and more detailed examination is necessary.

Third, agreement between data and synthetics with model 3DM-28 for the largest aftershock (M_W 6.3) and the aftershock that occurred on October 27 (M_W 5.8) is not satisfactory when compared with those of the main shock (Fig. 9c). We thought that the waveform modelling for the largest aftershock might be affected by the fact that the hypocentral depth was ∼6 km beneath the main shock. We then found that a low-velocity anomaly zone in the new tomography model 3DM-Kato08 from 15 to 20 km depth beneath the seismogenic zone was necessary to synthesize the data of the largest aftershock. This characteristic is reflected in model 3DM-28 (see Figs 5d and 6e). The velocity contrast between the hangingwall and footwall near the main shock hypocentre may be extended to the depth of the largest aftershock hypocentre ∼16 km or deeper, since the observed waveforms of the main shock and the largest aftershock have a resemblance. However, the fits between the observed and synthetic waveforms are not satisfactory yet because of the low-resolution of the local tomography model due to the hypocentral depth near the base of the seismogenic zone (Fig. 9c, top and middle).

The agreement between the data and the synthetics with model 3DM-28 for the aftershock on October 27 is relatively good on only a part of the footwall (Fig. 9c, bottom) for the low-resolution tomography model around the hypocentre of the event (see Fig. 5d, top). We think the structure situated more on the footwall side than the October 27 event may have been relatively less complex than that of the main shock. Since the largest aftershock and the October 27 event are located near the boundaries of the seismogenic zone in terms of depth and lateral distribution, further waveform modelling may be useful to understand the zone's vertical and lateral extents.

5 DISCUSSION

We constructed a 3-D velocity model, which could explain the waveform data by combining the 1D-FK, 3D-FD and DD tomography analyses, focusing on the structure around the seismogenic

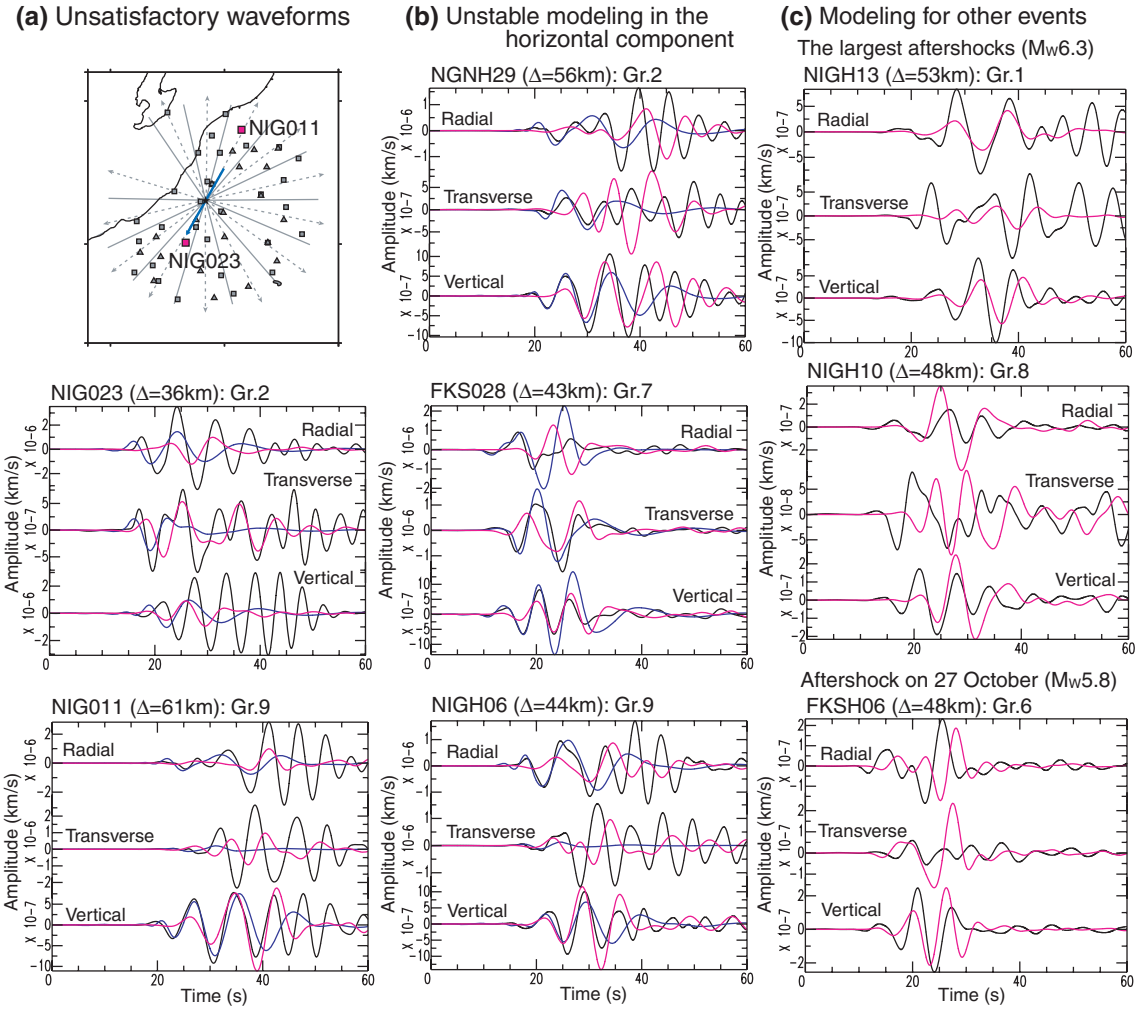

Figure 9. Examples of problems to be solved for model 3DM-28. (a) Unsatisfactory fit waveforms. (Top) Locations of stations NIG023 and NIG011, which are located on the boundary between the hanging and footwalls, that is, along the strikes of the major events. (Middle) Comparisons between three-component, bandpass-filtered ($0.05 \leq f \leq 0.2$ Hz) velocity data (black lines) and synthetic waveforms with each 1D-FK model (blue lines) and model 3DM-28 (pink lines), for the main shock recorded at station NIG023. The station ID, Δ and group number are given in the upper left-hand side the diagram. Top, middle and bottom traces in the diagram correspond to radial, transverse and vertical components, respectively. (Bottom) Same as middle, but at station NIG011. (b) Unstable modelling in the horizontal component. The horizontal data, same as middle in (a) but at stations NGNH29 (top), FKS028 (middle) and NIGH06 (bottom), have low-fits between the data and the synthetics although the vertical data at these stations have high-fits. (c) Waveform modelling for other large aftershocks. (Top) and (Middle) same as middle in (a), but with model 3DM-28 (pink lines) for the largest aftershock at stations NIGH13 on the hangingwall and NIGH10 on the footwall, respectively. (Bottom) Same as top and middle, but for the aftershock that occurred on 27 October at station FKSH06 on the footwall.

zone, in particular. The tomography inversion has resolution for short wavelength heterogeneities (grid-node ≥ 3 km^3) around the dense aftershock distribution due to the use of a large number of traveltime data, mainly from small aftershocks ($M \geq 1.2$), that is, high-frequency content of raw data ($f \geq \sim 1$ Hz) without amplitude information. In comparison, the 1D-FK and 3D-FD waveform modelling deal with relatively low-frequency content ($0.05 \leq f \leq 0.2$ Hz) of amplitudes and phases as well as traveltimes of the large events ($5.8 \leq M_{\rm W} \leq 6.6$) recorded within 80 km from the main shock epicentre. As explained in Appendix, the data have no or minimal effects of amplification due to scattering near the surface and are sensitive to the structure within a ∼40-km-horizontal distance from the epicentre and between ∼3 and 20 km in depth. We improved the 3D-FD structural model based on the new tomography model 3DM-Kato08 combined with the multiple 1D-FK models and derived model 3DM-28, which accounts for observed body waveforms, that is, amplitudes, phases and traveltimes. The agreement between the data and the synthetics calculated using the final model was satisfactory in all the groups.

Model 3DM-28 has the original velocity structure of model 3DM-Kato08 on the hangingwall with the thick sedimentary basin. However, on the footwall, the velocity increases of 5 or 10 per cent were required in the model to fit the data, especially in the source area with multiplanar faults (Fig. 6e). Fig. 5 shows vertical cross-section images at a right angle to the strike of the main shock (from $y = 0$ to +9 km shown in Fig. 6a, right-hand panel) for models 3DM-Kato06, 3DM-Kato08, 3DM-1 and 3DM-28. These are based, respectively, on the tomography image by Kato *et al.* (2006) (Fig. 4a), the new tomography image, the initial 3-D model (Fig. 6a) and the final improved model (Fig. 6e). Although the images shown in Fig. 5 have many different characteristics, the image produced by model 3DM-28 first shows a clearer contrast between low and high velocities on the hangingwall and footwall than that seen in the original tomography model, due to the higher velocity on the footwall.

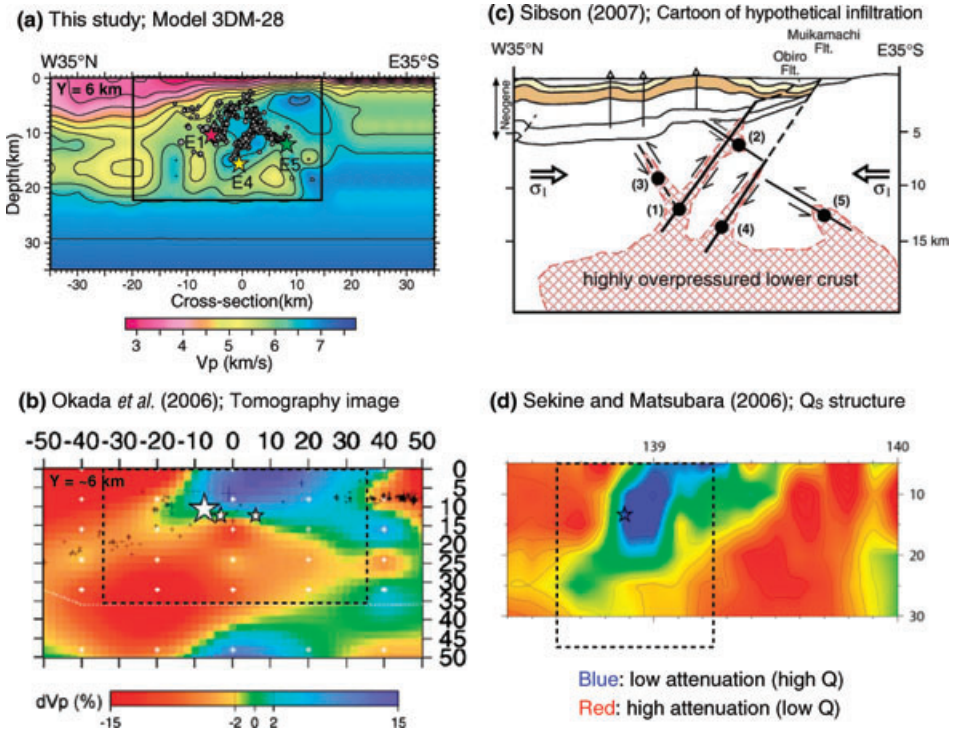

Figure 10. Comparison of the structural models. All the diagrams are the vertical cross-sections at right angles to the strike of the main shock. (a) Model 3DM-28 derived in this study. The area indicated by the inner box corresponds to the area illustrated in (c). (b) V_P perturbation ($-15 \leq dV_P \leq +15$ per cent) patterns of tomography model derived by Okada *et al*. (2006) using JMA traveltime data. The area indicated by the dotted inner box corresponds to the area shown in (a). (c) Schematic illustration of the hypothetical model of infiltration of pressured fluids by Sibson (2007). (d) Q_S structure estimated by Sekine & Matsubara (2006) using waveform maximum amplitudes. The area indicated by the dotted rectangle corresponds to the area shown in (a).

The vertical cross-section image of broader tomography model with approximately $-50 \leq (x, y) \leq +50$ and $0 \leq z \leq +50$ km (Okada *et al.* 2006) shows high-velocity anomalies ($+5 \leq \mathrm{d}V_P \leq +15$ per cent) in the seismogenic zone shallower than ∼15 km depth and wide low-velocity anomalies ($-5 \leq \mathrm{d}V_P \leq -15$ per cent) beneath the seismogenic zone from ∼15 to 40 km depth (Fig. 10b). Okada *et al.* (2006) suggest that the low-velocity areas represent the distribution of water rising from a greater depth due to upwelling flow within the mantle wedge. However, it seems to be difficult to envisage such large low-velocity anomalies in our model despite the high-velocity anomaly on the footwall surrounded by low-velocity anomalies. As described above, the low-velocity zones near the major faults revealed in the smaller scale model cannot be seen here because of the large grid intervals.

The vertical cross-section image of the broad Q_S structure determined using the maximum amplitude of waveforms (Sekine & Matsubara 2006) shows that the main shock occurred in a region with a distinct change in the Q_S structure, and the area of high Q_S (low attenuation) is situated on the southeastern (footwall) side (Fig. 10d). The high-Q_S image also corresponds to the region of aftershock distribution (e.g. Aoki *et al*. 2005; Shibutani *et al*. 2005; Kato *et al*. 2006) and shows similar contrasts to our velocity model. In our 3D-FD analysis, the heterogeneous Q structure was not considered. Even if the Q structure were to be considered, the characteristics of velocity structure in the improved model 3DM-28, such as the high-velocity anomaly around the seismogenic zone on the footwall, would not change, or rather high-velocity anomalies would become even stronger. From the broader image of model 3DM-28 as shown in Figs 5(d) and 10(a), our model can be characterized by individual high-velocity anomalies in the seismogenic zone surrounded by low-velocity anomalies.

In the narrow area of model 3DM-28 (the inner box in Fig. 10a), the velocity increases particularly in the seismogenic zone imply that there are certainly the low-velocity anomalies in the vicinity of the multiplanar faults, also shown in the original tomography models, but low-velocity anomalies may be small and exist locally. This also means that the low-velocity anomalies in the original tomography images (Figs 5a and b) inserted into the FD model appear indistinct, probably due to the grid node intervals of 3 km or larger and smoothing in the analyses. Furthermore, in the tomography the used stations are distributed densely within a radius of ∼30 km from the centre of the source region (see Kato *et al*. 2006), and the high-frequency data ($f \geq \sim 1$ Hz) of the small aftershocks are affected strongly by scattering near the ground surface, within the depth range shallower than ∼3 km. These may be related to the velocity increases required in the improvement of the 3D-FD model, but we cannot discuss directly the difference between velocity images derived using waveform modelling and tomography inversion because of the quite different frequency range adopted.

As shown in Fig. 10(a), the high-velocity zone located on the footwall, particularly around the multiplanar faults (E1, E4 and E5 planes), may represent the competent parts of the fault rupture zone (e.g. Lees 1990; Zhao *et al*. 1996). In particular, the area around the fault of the largest aftershock (E4) is a remarkably high-velocity zone. We think that the faster zone can be interpreted as a specially high-strength area that is required to rupture the E4 fault plain. The fault ruptured in only 40 min after the main shock (E1) and is parallel to the E1 plain at a distance of ∼6 km. The faster fault zone also seems to be consistent with the theory of mechanical lubrication applied by Brodsky & Kanamori (2001). In the lubricated fault, the permeability of the surrounding rock is sufficiently low enough to effectively confine fluids between the walls; fluid can flow into

a narrow fault core and the pore pressure dramatically increases. The localized participations of the fluids in the vicinity of the fault rupture zones surrounded by the dense, unfractured rock may be blurred or cannot be plainly revealed in our model based on the tomography images.

As described above, the 'unsatisfactory fit waveforms' recorded at stations along the strikes of the major faults seem to be generated as beating and could not be synthesized by our model. When two have similar frequencies to each other, the small difference in the frequency generates beating. From examinations in narrow frequency bands, the beating seems to be generated between 0.1 and 0.2 Hz. The waveform of the data bandpass-filtered between 0.05 and 0.1 Hz differs from that filtered in the range between 0.05 and 0.2 Hz. The locations of the major faults correspond to the boundary between the hangingwall with its thick sedimentary basin and the footwall in the basement of older rocks. However, the data at stations on the hangingwall (groups 1 and 13) were well synthesized using our 3-D model, and the unusual waveforms do not seem to be generated in the sedimentary basin at depths shallower than ∼6 km. These irregular waveforms may be generated by a local or thin anomalous (low-velocity) zone around the faults rupture (∼10 ± 5 km depth), immediately after the occurrence of the earthquake. Thus, the 'unsatisfactory fit waveforms' in this earthquake sequence, generated in the narrow frequency band ($0.1 \leq f \leq 0.2$ Hz), may be evidence of localized participation of fluids on the fault rupture plain, possibly in relation to the pulverized rock zone.

Moreover, the low-velocity anomaly zone within a depth range of 15–20 km beneath the seismogenic zone (lower crust) seems to be connected to the short wavelength low velocity anomalies at shallower depths (the inner box in Fig. 10a). The low-velocity anomaly in the lower crust was necessary to synthesize the waveforms of the largest aftershock. The revealed characteristics in and beneath the seismogenic zone may support an idea of infiltration of pressurized fluids from the lower crust into the multiplanar fault system, as proposed by Sibson (2007) and shown in Fig. 10(c). The steep dip angles of the fault planes of the main shock and the largest aftershock (50°–60°WNW) are poorly oriented for frictional reactivation, assuming the horizontal maximum compressive stress. On the other hand, the subsidiary faults of four other $M_W \geq 5.5$ aftershocks (25°–35°WNW) appear optimally oriented in the stress field. The combined reactivation of the unfavourably oriented reverse faults and optimally oriented thrusts requires high but probably variable fluid overpressuring within the rock-mass (Sibson 2007). In addition, Tajima & Tajima (2006, 2007) indicate that scaling relations between M_0 and corner frequency for a few foreshocks and a number of aftershocks ($3.5 \leq M_W \leq 4.0$) in this earthquake sequence are different between the on- and off-main fault events. They suggest that the different scaling relations for the small events may be related to local seismogenic conditions such as effects of fluid.

The aftershock activity in this earthquake sequence is extremely high when compared with that in other crustal earthquake sequences; the total M_0 release by the aftershocks reaches about 80 per cent of the main shock during the first few days (see Tajima & Tajima 2007, 2008). The aftershocks in this sequence seem to be clustered around each major fault (Fig. 1c). The characteristics of the aftershock activity may be affected by the complicated fault geometry related to the pressured fluids. The relation between the local effects of fluid overpressure beneath the seismogenic zone (∼15–20 km depth) with the low-velocity anomaly and the high-strength parts near the faults zone (∼3 to 15 km depth) with the high-velocity anomaly may have played a role in the rupture initiation and continuity of the large events ($M_W \geq 5.5$). Further examination with models that include such an influence as hypothesized by Sibson (2007) may be useful to understand the relationship between the seismogenic conditions and fluid distribution.

6 CONCLUSIONS

The 3-D velocity model around the source area of the 2004 mid-Niigata earthquake, 3DM-28, was constructed by carrying out waveform modelling and traveltime tomography inversion. The model satisfactorily explained the waveform data at most stations. Based on the analysis, we found the following characteristics:

(1) The images of the tomography model 3DM-Kato06 derived by Kato *et al*. (2006) and the new tomography model 3DM-Kato08 seem to be valid in the areas of high resolution, as the images are similar to each other within the used grid nodes (≥3 km). However, on the footwall of the main shock, which includes the multiplanar faults, the 3D-FD waveform modelling using only each tomography model was not sufficient to synthesize the observed waveforms in $0.05 \leq f \leq 0.2$ Hz at most stations.

(2) With increases of velocity on the footwall, the improved image produced by model 3DM-28 shows a clearer contrast between low- and high-velocities on the hangingwall and footwall of the main shock than that in the original tomography models.

(3) The original tomography models showed the low-velocity anomalies in the vicinity of the multiplanar faults. However, the velocity increases particularly near the seismogenic zone in model 3DM-28 imply that the low-velocity anomaly may be more locally restricted.

(4) The low-velocity anomaly zone within the depth range of 15–20 km beneath the seismogenic zone (lower crust) appears to be associated with the short-wavelength low-velocity anomalies at shallower depths (upper crust). These characteristics might support an idea of infiltration of pressurized fluids from the lower crust into the multiplanar fault system, as hypothesized by Sibson (2007).

(5) The 'unsatisfactory fit waveforms' recorded at stations along the strikes of the major faults seemed to be generated as beating and could not be synthesized by our model. Effects related to these waveforms may be further examined.

An approach using both of the seismic waveforms and the traveltimes is thus effective to examine a complicated structure like the source region of this earthquake sequence. We suggest that the clear velocity contrasts between the hangingwall and footwall and that between the upper crust and lower crust, together with the effect of fluid, seem to be an essential characteristic of the seismogenic condition with the multiplanar faults in this earthquake sequence.

ACKNOWLEDGMENTS

We thank S. Larsen for the use of the elastic FD code, E3D (Larsen & Schultz 1995). We also thank L. Boschi and an anonymous reviewer for providing valuable review comments to improve the clarity of the manuscript. The high performance computer time was provided by the Earth Simulator Center, the Japan Agency for Marine-Earth Science and Technology and the Information Media Center, Hiroshima University. We used the F-net event catalogue assembled by NIED and the waveform data collected at the K-NET and KiK-net stations operated by NIED. The figures were prepared using the Generic Mapping Tools by Wessel & Smith (1995). This study was partially supported by a Research Fellowship for Young Scientists

No. 19·4077 (for RT) from the Japan Society for the Promotion of Science.

REFERENCES

Aoki, S., Nishi, M., Nakamura, K., Hashimoto, T., Yoshikawa, S. & Ito, H.M., 2005. Multi-planar structures in the aftershock distribution of the Mid Niigata prefecture Earthquake in 2004, *Earth Planet. Space,* **57,** 411–416.

Brodsky, E.E. & Kanamori, H., 2001. Elastohydrodynamic lubrication of faults, *J. geophys. Res.,* **106,** 16 357–16 374.

Fukuyama, E., Ishida, M., Dreger, D.S. & Kawai, H., 1998. Automated seismic moment tensor determination by using on-line broadband seismic waveforms (in Japanese with an English abstract), *Zisin, 2nd Ser.,* **51,** 149–156.

Furumura, T. & Hayakawa, T., 2007. Anomalous propagation of long-period ground motions recorded in Tokyo during the 23 October 2004 M_w 6.6 Niigata-ken Chuetsu, Japan, Earthquake, *Bull. seism. Soc. Am.,* **97,** 863–880, doi:10.1785/0120060166.

Hayashida, T. & Tajima, F., 2007. Calibration of amplification factors using KiK-net strong-motion records: toward site effective estimation of seismic intensities, *Earth Planet. Space,* **59,** 1111–1125.

Hikima, K. & Koketsu, K., 2005. Rupture processes of the 2004 Chuetsu (mid-Niigata prefecture) earthquake, Japan: a series of events in a complex fault system, *Geophys. Res. Lett.,* **32,** L18303, doi:10.1029/2005GL023588.

Honda, R., Aoi, S., Morikawa, N., Sekiguchi, H., Kunugi, T. & Fujiwara, H., 2005. Ground motion and rupture process of the 2004 Mid Niigata Prefecture earthquake obtained from strong motion data of K-NET and KiK-net, *Earth Planet. Space,* **57,** 527–532.

Kato, A. *et al*., 2005. Short-term spatiotemporal variations in the aftershock sequence of the 2004 mid-Niigata prefecture earthquake, *Earth Planet. Space,* **57,** 551–556.

Kato, A., Sakai, S., Hirata, N., Kurashimo, E., Iidaka, T., Iwasaki, T. & Kanazawa, T., 2006. Imaging the seismic structure and stress field in the source region of the 2004 mid-Niigata prefecture earthquake: structural zones of weakness and seismogenic stress concentration by ductile flow, *J. Geophys. Res.,* **111,** B08308, doi:10.1029/2005JB004016.

Kato, A. & The Research Team of aftershock observations for the 2004 mid-Niigata Prefecture Earthquake, 2007. High-resolution aftershock observations in the source region of the 2004 mid-Niigata Prefecture Earthquake, *Earth Planet. Space,* **59,** 923–928.

Korenaga, M., Matsumoto, S., Iio, Y., Matsushima, T., Uehira, K. & Shibutani, T., 2005. Three dimensional velocity structure around aftershock area of the 2004 mid Niigata prefecture earthquake (M6.8) by the Double-Difference tomography, *Earth Planet. Space,* **57,** 429–433.

Larsen, S. & Schultz, C.A., 1995. ELAS3D: 2D/3D elastic finite difference wave propagation code, Technical report, No. UCRL-MA-121792, 19 pp.

Lees, J.M., 1990. Tomographic P-wave velocity images of the Loma Prieta earthquake asperity, *Geophys. Res. Lett.,* **17,** 1433–1436.

Niigata prefecture, 2000. Niigata prefecture (in Japanese), in *Geological Map of Niigata prefecture (2000) 1:200 000 and Explanatory Texts,* eds Kobayashi, I.

Okada, T., Yaginuma, T., Umino, N., Matsuzawa, T., Hasegawa, A., Zhang, H. & Thurber, C.H., 2006. Detailed imaging of the fault planes of the 2004 Niigata–Chuetsu, central Japan, earthquake sequence by double-difference tomography, *Earth planet. Sci. Lett.,* **244,** 32–43.

Sagiya, T., Miyazaki, S. & Tada, T., 2000. Continuous GPS array and present-day crustal deformation of Japan, *Pure appl. Geophys.,* **157,** 2303–2322.

Saikia, C.K., 1994. Modified frequency-wavenumber algorithm for regional seismograms using Filon's quadrature: modeling Lg waves in eastern North America, *Geophys. J. Int.,* **118,** 142–158.

Sato, H., 1994. The relationship between late Cenozoic tectonic events and stress field and basin development in northeast Japan, *J. geophys. Res.,* **99,** 22 261–22 274.

Sekine, S. & Matsubara, M., 2006. Three dimensional velocity and attenuation structure around the mid Niigata region (in Japanese), *Chikyu Mont.,* **53,** 27–33.

Shibutani, T. *et al*., 2005. Aftershock distribution of the 2004 Mid Niigata Prefecture Earthquake derived from a combined analysis of temporary online observations and permanent observations, *Earth Planet. Space,* **57,** 545–549.

Sibson, R.H., 2007. An episode of fault-valve behavior during compressional inversion?—the 2004 M_j 6.8 Mid-Niigata Prefecture, Japan earthquake sequence, *Earth planet. Sci. Lett.,* **257,** 188–199.

Tajima, F. & Grand, S.P., 1998. Variation of transition zone high velocity anomalies and depression of the 660km discontinuity associated with subduction zones from the southern Kuriles to Izu-Bonin, *J. geophys. Res.,* **103**(B7), 15 015–15 036.

Tajima, F. & Nakagawa, T., 2006. Implications of seismic waveforms: complex physical properties associated with stagnant slab, *Geophys. Res. Lett.,* **33,** L03311, doi:10.1029/2005GL024314.

Tajima, R. & Tajima, F., 2006. The 2004 Mid Niigata prefecture earthquake: characterization of the aftershock area using a spectral ratio analysis (in Japanese with an English abstract), *Zisin, 2nd Ser.*, **58,** 445–455.

Tajima, R. & Tajima, F., 2007. Seismic scaling relations and aftershock activity from the sequences of the 2004 mid Niigata and the 2005 west off Fukuoka earthquakes (M_W 6.6) in Japan, *J. geophys. Res.,* **112,** B10302, doi:10.1029/2007JB004941.

Tajima, R. & Tajima, F., 2008. Seismic scaling relation of the 2007 Off Mid Niigata, Japan, earthquake (M_W 6.6) sequence in comparison with two other earthquake (M_W 6.6) sequences, *Earth Planet. Space,* **60,** 1137–1141.

Tajima, F., Fukao, Y., Obayashi, M. & Sakurai, T., 1998. Evaluation of slab images in the northwestern Pacific, special issue of the Ocean Hemisphere Project symposium, *Earth Planet. Space,* **50** (11 & 12), 953–964.

Takeuchi, K., Yanagisawa, Y., Miyazaki, J. & Ozaki, M., 2004. *1:50 000 digital Geological Map of the Uonuma region, Niigata Prefecture (Ver. 1)* (in Japanese with an English abstract),Vol. 412, Geological Survey of Japan.

Ueno, H., Hatakeyama, S., Aketagawa, T., Funasaki, J. & Hamada, N., 2002. Improvement of hypocenter determination procedures in the Japan Meteorological Agency (in Japanesewith an English abstract), *Quater. J. Seismol.,* **65,** 123–134.

Wessel, P. & Smith, W.H.F., 1995. New version of the Generic Mapping Tools released, *EOS. Trans. Am. geophys. Un.,* **76,** 329.

Yagi, Y., 2005. Source process of the 2004 Mid Niigata prefecture earthquake obtained by joint Inversion of near-field and teleseismic,in *Proceedings of the Joint Meeting for Earth and Planetary Science (Abstract),* Japan, S101–P001.

Zhang, H. & Thurber, C.H., 2003. Double-difference tomography: the method and its application to the Hayward fault, California, *Bull. seism. Soc. Am.,* **93,** 1875–1889.

Zhao, D., Kanamori, H., Negishi, H. & Wiens, D., 1996. Tomography of the source area of the 1995 Kobe earthquake: evidence for fluids at the hypocenter?, *Science,* **274,** 1891–1894.

APPENDIX: EXAMINATION OF AMPLIFICATION EFFECTS NEAR THE SURFACE AND RAY PATHS IN THE DIFFERENT STRUCTURE

We compared the waveform data recorded at the ground surface located (K-NET and KiK-net) and borehole situated (KiK-net) stations, with the different frequency bands, to examine effects of amplification near the surface. As shown in Fig. A1, we could make sure that the waveforms in $0.05 \leq f \leq 0.2$ Hz have less effects of amplification due to scattering near the surface. We also checked how the first arrival *P*-waves sample the different velocity structures from the sources of main shock (10 km depth) or the largest aftershock (16 km depth) to stations located within a distance of ∼80 km. The rays strongly sample the structure between ∼3 and 20 km depth within the distance (Fig. A2).

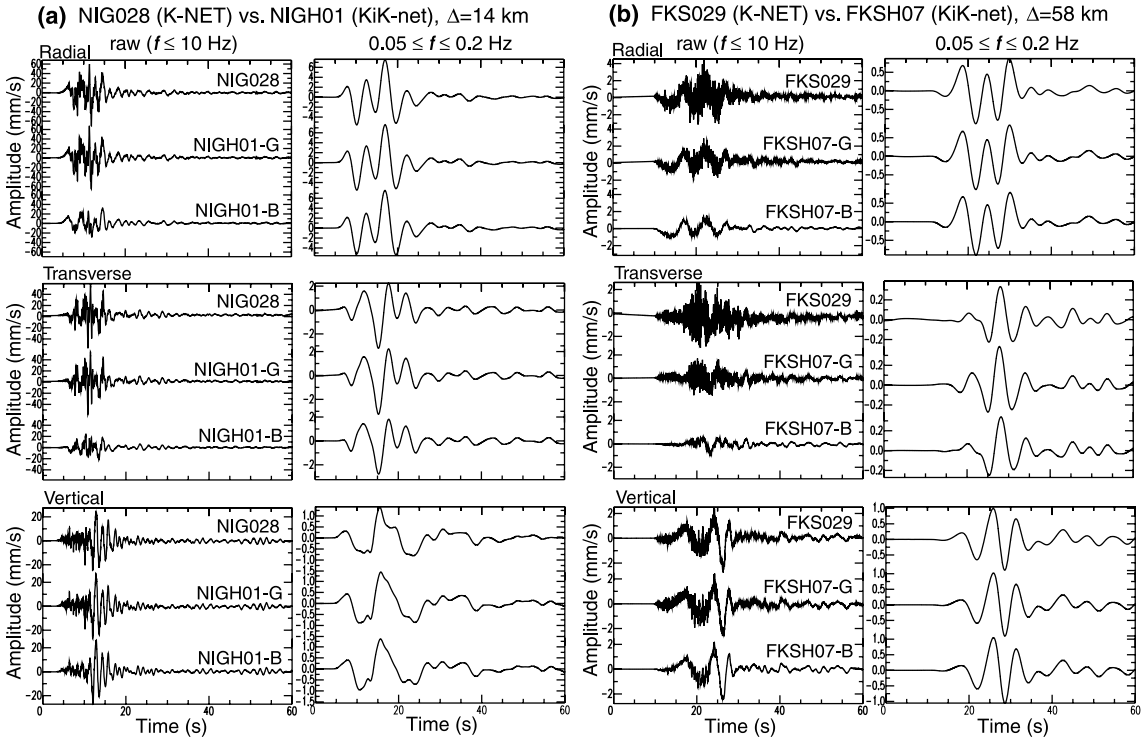

Figure A1. Comparison between raw (left-hand panel) and bandpass filtered between 0.05- and 0.2-Hz (right-hand panel) velocity waveforms recorded at ground surface (K-NET and KiK-net) stations and borehole (KiK-net) stations that are set almost same location as shown in Fig. 1(a). (a) At stations NIG028 (K-NET) versus NIGH01 (KiK-net), with $\Delta = 14$ km. Top, middle and bottom traces in each diagram correspond to the waveforms at ground surface K-NET station NIG028 and round surface and borehole KiK-net stations NIGH01 (-G and -B), respectively. Top, middle and bottom diagrams correspond to the waveforms in the radial, transverse and vertical components, respectively. (b) Same as (a), but at stations FKS029 (K-NET) versus FKSH07 (KiK-net), with $\Delta = 58$ km.

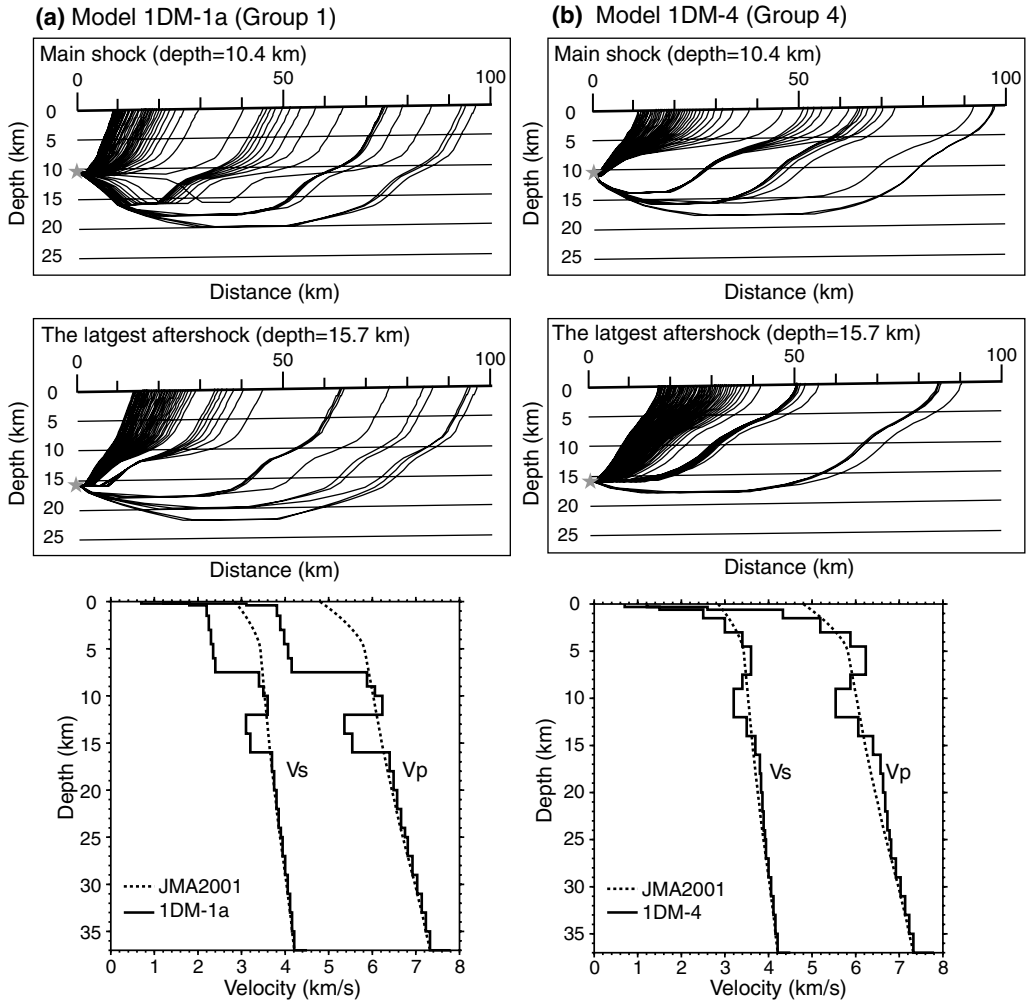

Figure A2. Illustration of seismic rays of first arriving *P* waves from source depths of the main shock (10 km) and the largest aftershock (16 km) to stations within the distance of ∼100 km. (a) Rays calculated using 1D-FK model 1DM-1a (see Fig. 2a). Top, middle and bottom diagrams correspond to the rays from the sources of the main shock and the largest aftershock and used seismic velocity model 1DM-1a, respectively. (b) Same as (a), but using model 1DM-4 (see Fig. 2b).